NANO LETTERS

2007
Vol. 7, No. 4
880−884

Wavelength Selective Nanophotonic Components Utilizing Channel Plasmon Polaritons

Valentyn S. Volkov,*,† Sergey I. Bozhevolnyi,† Eloïse Devaux,‡ Jean-Yves Laluet,‡ and Thomas W. Ebbesen‡

Department of Physics and Nanotechnology, Aalborg University, Skjernvej 4A, DK-9220 Aalborg Øst, Denmark, and Laboratoire des Nanostructures, ISIS, Université Louis Pasteur, 8 allée Monge, BP 70028, 67083 Strasbourg, France

Received January 26, 2007

ABSTRACT

We fabricate and investigate wavelength selective components utilizing channel plasmon polaritons (CPPs) and operate at telecom wavelengths: a waveguide-ring resonator-based add-drop multiplexer (WRR-ADM) and a compact (3.75-μm-long) Bragg grating filter (BGF). The CPP waveguides represent 0.5-μm-wide and 1.3-μm-deep V-grooves in gold, which are combined with a 5-μm-radius ring resonator (in the WRR-ADM) or 0.5-μm-long wells milled with the period of 0.75 μm across a groove (in the BGF). The CPP-based components are characterized in the wavelength range of 1425–1600 nm by use of near-field optical microscopy, exhibiting the wavelength selectivity of ~40 nm.

Channel plasmon polaritons (CPPs) are electromagnetic waves that are bound to and propagate along the bottom of grooves cut into a metal.[1] They are expected to exhibit useful subwavelength confinement, relatively low propagation loss, and single mode operation[1,2] as well as efficient transmission around sharp bends.[3] Our previous experiments showed that the CPPs at telecom wavelengths propagate over tens of micrometers along grooves in gold and exhibit strong subwavelength confinement[4] along with low bend losses in large-angle S-bends and Y-splitters,[5] thereby enabling the realization of ultracompact plasmonic components, such as Mach−Zehnder interferometers and waveguide-ring (WR) resonators.[6] The results obtained with the above set of structures encouraged us to further exploit the potential of CPPs and to investigate more sophisticated and/or new functional plasmonic components. In this letter, we report the fabrication and investigation of CPP-based wavelength selective components: a WR resonator-based add-drop multiplexer and a compact Bragg grating filter (BGF).

The experimental setup employed in this work for the CPP observation and characterization is essentially the same as that used in our previous experiments.[4−6] It consists of a collection scanning near-field optical microscope (SNOM) with an uncoated sharp fiber tip used as a probe and an arrangement for launching tunable (1425−1600 nm) transverse electric (TE)-polarized (the electric field is parallel to the sample surface plane) radiation into a metal groove by positioning a tapered-lensed polarization-maintaining single mode fiber (Figure 1a). The adjustment of the in-coupling fiber with respect to the sample facet was accomplished when monitoring the light propagation along the sample surface with help of a far-field microscopic arrangement in which the CPP scattering (out of the surface plane) was producing the track of radiation propagating along a groove.[4] It should be also noted that in the course of our SNOM experiments, we routinely verified that the detected signal is primarily related to the total CPP field intensity distribution along the groove structures area by recording optical images at different fiber tip−surface distances.[5] The sample containing V-grooves with the angles close to ~25° and depths of ~1.3 μm has been fabricated (using a focused ion-beam milling technique) in a 1.9-μm-thick gold layer deposited on a substrate of fused silica covered with an 80-nm-thick indium-tin-oxide layer. Special care has been taken to fabricate V-grooves with smooth walls and prevent contamination of the completed structures with dust particles.

As a first example, we have chosen a WR resonator-based add-drop multiplexer (WRR-ADM) arrangement that is expected to demonstrate relatively high drop efficiency.[7] In the design of WRR-ADM, we used a 5-μm-radius ring and the same V-groove waveguides. The groove profiles turned out to be similar to triangular ones (see scanning electron image (SEM) inset in Figure 1a). It is also seen that the groove walls are somewhat rough, a feature that can influence the CPP propagation by causing the CPP scattering out of

* To whom correspondence should be addressed. E-mail address: volkov@physics.aau.dk.
† Aalborg University.
‡ Université Louis Pasteur.

10.1021/nl070209b CCC: $37.00
Published on Web 03/13/2007

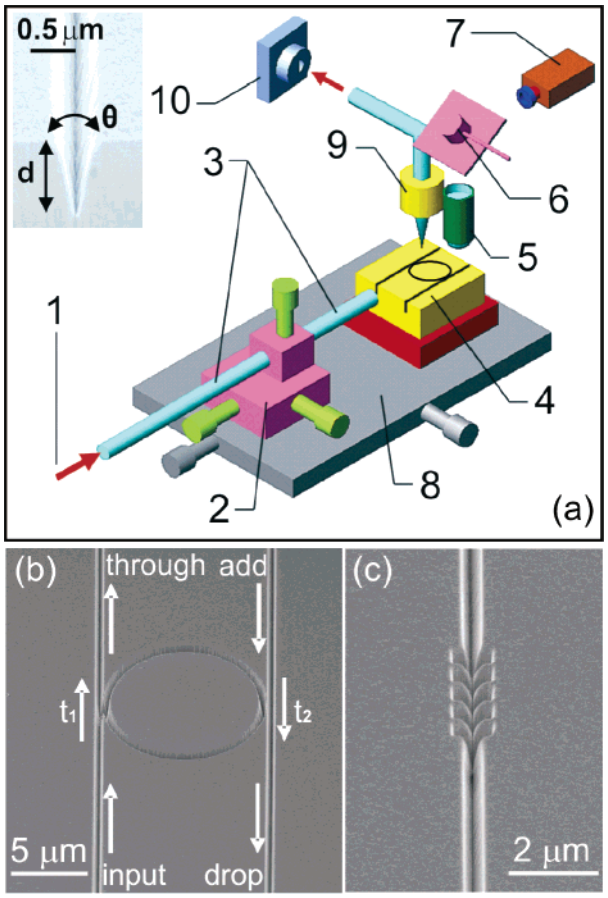

Figure 1. (a) Schematic layout of the experimental setup: (1) TE-polarized radiation from tunable laser (1425−1600 nm); (2) X, Y, Z stage; (3) input fiber; (4) sample; (5) microscope objective; (6) mirror; (7) IR vidicon; (8) X, Y stage; (9) SNOM head; (10) InGaAs photoreceiver. Inset in (a), SEM image showing typical groove profile (d and θ are the groove depth and angle, respectively). (b) SEM image of the investigated WRR-ADM composed of two triangular gold grooves combined with 5-μm-radius waveguide-ring resonator. (c) SEM image of the investigated BGF composed of 750-nm-period structure composed of 5 wells cut across the input V-groove.

the groove. The main system parameters are transmission coefficients, t_1 and t_2, through the coupling regions (Figure 1b) and the transmission around the ring, $\alpha \exp(i\theta)$. The power transmissions in the through (P_T) and drop (P_D) channels of WRR-ADM under the condition that a single unidirectional mode of the ring resonator is excited are given by[8]

$$P_T = \frac{(\alpha t_2)^2 + t_1^2 - 2\alpha t_1 t_2 \cos\theta}{1 + (\alpha t_1 t_2)^2 - 2\alpha t_1 t_2 \cos\theta},$$

$$P_D = \frac{(1 - t_1^2)(1 - t_2^2)\alpha}{1 + (\alpha t_1 t_2)^2 - 2\alpha t_1 t_2 \cos\theta},$$

$$\theta = \frac{2\pi}{\lambda} N_{\text{eff}} 2\pi R \qquad (1)$$

where we neglected losses in the system except for during the propagation in the ring. R is the ring radius, N_{eff} is the CPP effective index, and λ is the light wavelength in air. It is seen that the power transmissions are out of phase and

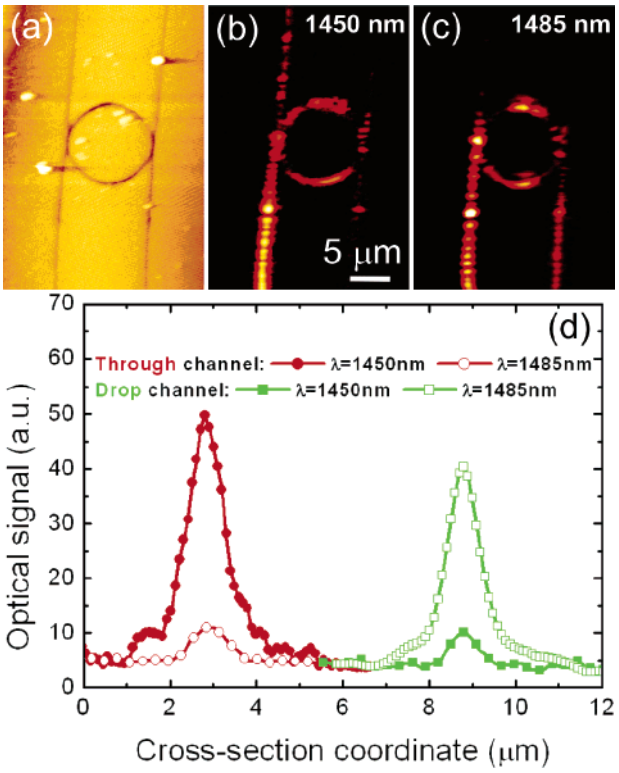

Figure 2. Pseudocolor (a) topographical and (b, c) near-field optical images (25 × 35 μm^2) obtained with the investigated WRR-ADM at $\lambda \cong$ (b) 1450 and (c) 1485 nm. (d) Normalized cross sections obtained from the optical images shown in (b) and (c) for two different output (through and drop) channels with the signal being normalized to be at the same level in the input channel.

periodic with respect to the phase θ accumulated by the CPP mode per circulation, implying the possibility of wavelength adding and dropping. Our main interest was in verifying the principal possibility of realization of a plasmonic WRR-ADM, achieving thereby the wavelength division and multiplexing functionality with CPPs.

The typical near-field optical images obtained with the transmitted (through) light power at maximum and minimum are shown in Figure 2 along with the corresponding normalized cross sections for two different wavelengths, exhibiting a clear difference in the transmitted CPP power for different output (through and drop) channels. The signal cross sections made at the intensity maxima are very close to the Gaussian distributions in shape with the full width at half-maximum of ∼900 nm (Figure 2d). It is also seen that the signal does not go to zero outside the groove indicating the presence of a homogeneous background at the level of ∼10% compared to the maximum signal. However, it is not clear to what extent it influences the signal measured in the middle of a groove with the SNOM fiber tip being actually below the sample surface by ∼40 to 100 nm, depending on the groove and tip shapes. Similar cross sections were used to evaluate the normalized outputs (in the through and drop channels) for the investigated WRR-ADM as a function of the light wavelength. The data obtained for both output channels were fitted with the dependences calculated according to eq 1 demonstrating quite good agreement (Figure 3). When fitting, we used the following CPP parameters: $N_{\text{eff}} = 1.015$, $\alpha =$

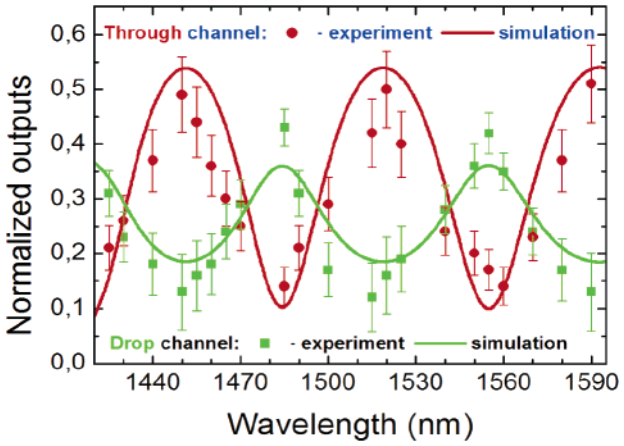

Figure 3. WRR-ADM transmission spectra obtained for the through and drop channels along with the fitted curves corresponding to the modeled WRR-ADM response. The output-to-input ratio obtained by using average (along 10 lines) cross sections of near-field optical images (similar to that shown in Figure 2) for both channels. The error bars are estimated from the maximum variation in the ratio when placing the averaging windows at different positions along the input and output channels.

0.71 (which are close to the values used previously[6] and are calculated by using the effective-index approximation,[9] neglecting the bend loss), and allowed for small variations in the ring radius R. The fitted values were found to be $t_1 \cong 0.31$, $t_2 \cong 0.78$, and $R \cong 5.12$ μm, which were consistent with the previous experiments[6] and with the investigated WRR-ADM configuration. In particular, one notices that the ring-channel separation is smaller (by ~100 nm) at the input-through channel compared to that at the add-drop channel (Figure 1b), implying the transmission should be larger in the latter (i.e., t_2 should be larger than t_1 as was deduced during the fitting procedure). Such a sensitivity of the WRR-ADM performance with respect to the system parameters implies stringent requirements on the fabrication, a feature that is in fact typical also for (conventional) compact photonic components based on high-index-contrast (photonic wire) waveguides.[10] Note that the suppression of the dropped wavelength in the through channel is quite large (on average, ~5) allowing for the efficient wavelength filtering with the bandwidth of ~40 nm.

Our next step was to try out one of the simplest wavelength-sensitive waveguide component, a BGF. A conventional waveguide BGF incorporates typically a periodic stack of layers made of materials with different optical refractive indexes.[11] The CPP propagating along a metal groove features the subwavelength confinement and effective refractive index larger than that in air,[1−4] implying the impedance mismatch with the propagating in free space modes. Our idea was to periodically mill deep and wide wells across a V-groove, forcing the CPP mode to "jump" over free space junctions (Figure 1c) and to experience periodic reflections (as well as out-of-plane scattering) that can eventually add up to the efficient reflection and filtering at the Bragg wavelength. It was also clear that a compromise should be sought between the filter efficiency and scattering loss, both being proportional to the number of periods. A

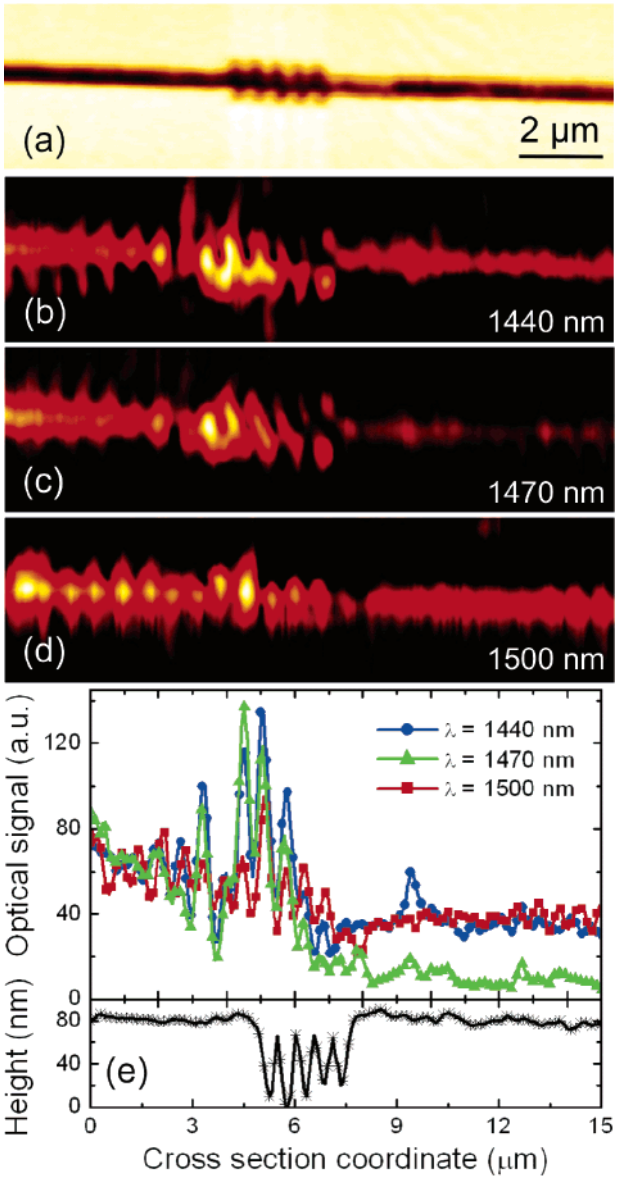

Figure 4. Pseudocolor (a) topographical and (b−d) near-field optical images (15 × 4 μm^2) obtained with the investigated BGF at $\lambda \cong$ (b) 1440, (c) 1470 nm, and (d) 1500 nm. (e) Corresponding cross sections (averaged along 10 lines along the CPP propagation direction) of the topographical (stars) and near-field optical images (filled circles, triangles, and squares) shown in (a−d), respectively.

750-nm-period BGF configuration consisting of five 500-nm-long and 1-μm-wide wells was fabricated using the usual design of V-grooves (Figure 1c).

The SNOM images recorded for different light wavelengths demonstrate clearly the filtering effect, showing strong attenuation in transmission of the CPP at the wavelength of ~1470 nm (Figure 4), which is close to the double BGF period as expected. Note that the near-field optical images are rather complicated reflecting interference between the propagating CPP (incident on the BGF), the CPP reflected by the BGF structure, and free-space propagating field components scattered at the fiber−CPP coupling and by the BGF well-groove junctions. The scattering processes occur at all wavelengths, resulting in the signal increase

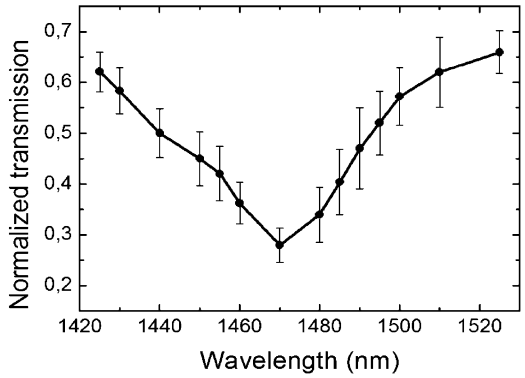

Figure 5. BGF transmission spectra representing the output-to-input ratio obtained by using average (along 10 lines) cross sections of near-field optical images (similar to that shown in Figure 4) taken perpendicular to the CPP propagation direction before and after the BGF. The error bars are estimated from the maximum variation in the ratio when placing the averaging windows at different positions along the groove regions (before and after the grating).

inside the BGF region and the BGF insertion loss, whereas the Bragg reflection is most pronounced at the filter wavelength of 1470 nm, leading to stronger signal oscillations before and inside the BGF as well as to the attenuation in transmission (Figure 4e).

We have further evaluated the transmission spectra (the corresponding output-to-input ratio as a function of the light wavelength) for the investigated BGF by making the optical image average cross sections perpendicular to propagation direction (Figure 5). It is seen that the transmission dip is surprisingly well pronounced and narrow for such a short (3.75-μm-long) BGF. When applying a periodic-layered media approach[12] for modeling the BGF, we could not get a reasonable agreement between the measured and simulated transmission spectra no matter what refractive indexes were used. At present, we cannot thereby offer an explanation of the measured spectrum, but it could be related to more complicated physical phenomena (e.g., cavity effects) involved in the process of CPP interaction with the periodic structure of wells. However, we would rather desist from definite conclusions before conducting further detailed investigations, including accurate modeling of the CPP propagation along metal grooves containing periodic wells, which are needed to verify this conjecture.

To verify the occurrence of the Bragg reflection of the incident CPP at the transmission minimum, we have studied the spatial-frequency spectra in the near-field optical images cut along the CPP propagation direction. The typical spatial-frequency spectra obtained before and after the BGF area for two different wavelengths (Figure 6) exhibit significant differences in heights of the peak approximately corresponding to half of the CPP wavelength (peak P_1 at ~712 nm). A very pronounced peak P_1 dominating the spectrum for the incoming CPP at $\lambda \cong 1460$ nm (that is close to the Bragg resonance) might be explained by the efficient CPP reflection from the periodic structure (Figure 6a). This peak is virtually absent in the spectrum of the optical signal distribution recorded after the BGF for both wavelengths and is barely seen for the incoming spatial spectrum obtained at $\lambda \cong 1495$ nm, implying weak CPP reflection (Figure 6b). On the other hand, our analysis of the spatial spectra for different wavelengths has shown that the situation is quite complicated, because these spectra exhibit also several other features that are independent of the light wavelength (e.g., spectral peaks P_2 and P_3 on Figure 6) and are probably related to the roughness of groove walls.[4]

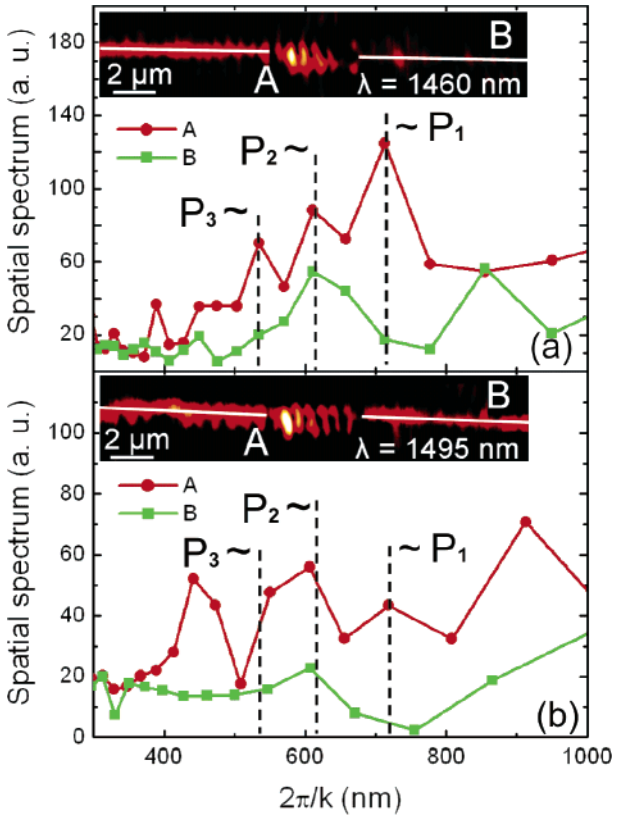

Figure 6. Spatial-frequency spectra obtained with near-field optical images (shown in the insets) straight regions of the groove before and after (along the lines marked with A and B) the BGF at $\lambda \cong$ (a) 1460 and (b) 1495 nm. Positions of the main peaks dominating the spectrum are indicated with dashed lines. The size of the inset optical image is 20 × 4 μm^2.

In summary, we have realized and demonstrated high performance of CPP-based wavelength selective nanophotonic components operating at telecom wavelengths: the WRR-ADM composed of two 0.5-μm-wide and 1.3-μm-deep gold grooves combined with a 5-μm-radius ring resonator and a compact (3.75-μm-long) BGF comprised 0.5-μm-long wells milled with the period of 0.75 μm across a groove. High quality SNOM images of the components have been obtained in the wavelength range of 1425−1600 nm and analyzed to determine their characteristics. For the WRR-ADM, the suppression of the dropped wavelength was found to be quite large (on average, ~5) allowing for the efficient wavelength filtering with the bandwidth of ~40 nm. The BGF made of only 5 wells has been shown to suppress the transmitted CPP power by a factor of ~3 at the Bragg wavelength. Finally, we should mention that the performance of considered plasmonic structures can be further improved by perfecting the quality of fabricated grooves (especially groove walls) and optimizing geometrical parameters.

Acknowledgment. The authors gratefully acknowledge financial support from the European Network of Excellence, PLASMO-NANO-DEVICES (FP6-2002-IST-1-507879), and STREP SPP (FP6-NMP4-CT-2003-505699).

References

(1) Novikov, I. V.; Maradudin, A. A. *Phys. Rev. B* **2002**, *66*, 035403.
(2) Moreno, E.; Garcia-Vidal, F. J.; Rodrigo, S. G.; Martin-Moreno, L.; Bozhevolnyi, S. I. *Opt. Lett.* **2006**, *23*, 3447.
(3) Pile, D. F. P.; Gramotnev, D. K. *Opt. Lett.* **2005**, *30*, 1186.
(4) Bozhevolnyi, S. I.; Volkov, V. S.; Devaux, E.; Ebbesen, T. W. *Phys. Rev. Lett.* **2005**, *95*, 046802.
(5) Volkov, V. S.; Bozhevolnyi, S. I.; Devaux, E.; Ebbesen, T. W. *Appl. Phys. Lett.* **2006**, *89*, 143108.
(6) Bozhevolnyi, S. I.; Volkov, V. S.; Devaux, E.; Laluet, J.-Y.; Ebbesen, T. W. *Nature* **2006**, *440*, 508.
(7) Xiao, S.; Qiu, M. *Opt. Express* **2006**, *14*, 2932.
(8) Choi, J. M.; Lee, R. K.; Yariv, A. *Opt. Lett.* **2002**, *27*, 1598.
(9) Bozhevolnyi, S. I. *Opt. Express* **2006**, *14*, 9467.
(10) Xia, F.; Sekaric, L.; Vlasov, Y. *Natur. Photon.* **2007**, *1*, 65.
(11) Lee, D. L. *Electromagnetic Principles of Integrated Optics*; John Wiley: NY, 1986.
(12) Yariv, A.; Yeh, P. *Optical Waves in Crystals*; John Wiley: NY, 1984.

NL070209B